A Long Wavelength Model for Manufacturing of Continuous Metal Microwires by Thermal Fiber Drawing From a Preform

Jingzhou Zhao
Department of Mechanical and Aerospace Engineering,
University of California, Los Angeles,
404 Westwood Plaza,
Los Angeles, CA 90095;
Department of Mechanical Engineering,
Western New England University,
1215 Wilbraham Road,
Springfield, MA 01119
e-mails: Jingzhou.zhao@ucla.edu;
Jingzhou.zhao@wne.edu

Xiaochun Li[1]
Department of Mechanical and Aerospace Engineering,
University of California, Los Angeles,
404 Westwood Plaza,
Los Angeles, CA 90095
e-mail: xcli@seas.ucla.edu

Thermal drawing from a preform recently emerges as a scalable manufacturing method for the high volume production of continuous metal microwires for numerous applications. However, no model can yet satisfactorily provide effective understanding of core diameter and continuity from process parameters and material properties during thermal drawing. In this paper, a long wavelength model is derived to describe the dynamics of a molten metal micro-jet entrained within an immiscible, viscous, nonlinear free surface extensional flow. The model requires numerical data (e.g., drawing force and cladding profile) be measured in real time. Examination of the boundary conditions reveals that the diameter control mechanism is essentially volume conservation. The flow rate of molten metal is controlled upstream while the flow velocity is controlled downstream realized by solidification of the molten metal. The dynamics of the molten metal jet are found to be dominated by interfacial tension, stress in the cladding, and pressure in the molten metal. Taylor's conical fluid interface solution (Taylor, 1966, "Conical Free Surfaces and Fluid Interfaces," Applied Mechanics, Springer, Berlin, pp. 790–796.) is found to be a special case of this model. A dimensionless capillary number $Ca = 2Fa/\gamma A(0)$ is suggested to be used as the indicator for the transition from continuous mode (i.e., viscous stress dominating) to dripping mode (i.e., interfacial tension dominating). Experimental results showed the existence of a critical capillary number Ca_{cr}, above which continuous metal microwires can be produced, providing the first ever quantitative predictor of the core continuity during preform drawing of metal microwires. [DOI: 10.1115/1.4038433]

Introduction

Thermal drawing from a preform recently emerges as a scalable manufacturing method for the high volume production of continuous metal microwires, in a way very similar to continuous casting, but at a much smaller length scale. Indefinitely, long metal wires are produced by melting, forming, and then solidifying directly from bulk metal, with the help of a deformable "mold" made of an amorphous cladding material (e.g., usually made of thermoplastic or glass).

During a typical fiber drawing process, as shown in Fig. 1, the metal embedded preform is aligned and fixed under a preform chuck, which is then slowly lowered into a furnace (sometimes an induction coil) which temperature is carefully controlled and stabilized at a designated value. After the heated preform in the furnace necks down under its own weight (or under external pulling forces sometimes), the bottom portion of the preform is cut away and the fiber is fed through a pinch wheel. The produced fiber filament is ultimately winded onto a spool. The diameter of the fiber D_f is usually measured by a laser diameter. The draw-down ratio D_r is defined as the ratio between the fiber pulling speed $U(L)$ and preform feeding speed $U(0)$. At steady-state, the law of mass conservation requires $D_r \equiv U(L)/U(0) = (D_p/D_f)^2$, where D_p is the preform diameter. The drawing force or fiber tension, which is often monitored by a load cell, is also an important control parameter and measures the tensile stress along the fiber.

Material selection criteria can be found in the literature [1,2] and are summarized here:

(1) The viscosity of the most viscous constituent material (i.e., the cladding) should fall between $10^{3.5}$ and 10^7 Poise at the drawing temperature for the process to be controllable. Amorphous materials, such as glass and polymers, are typically used as the support (cladding).
(2) The melting temperature of the core metal (T_m) should be lower than or at least overlap with the drawing temperature (T). Low vapor pressure of the metal is desired and its boiling should be avoided.
(3) Chemical reactions between the cladding and core materials should be avoided unless intentionally designed, e.g., for in-fiber synthesis purposes [3].
(4) It is desired that cladding and core materials exhibit good adhesion/wetting with each other during and after drawing

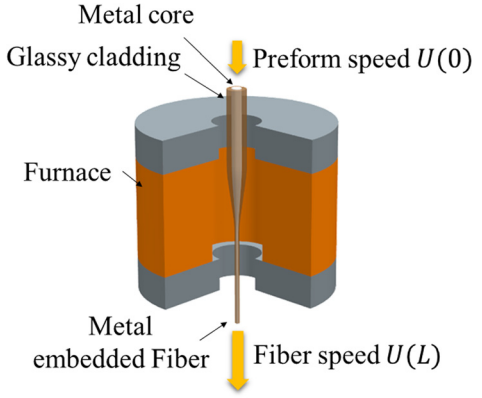

Fig. 1 Schematic and process parameters of metal core fiber drawing from a preform

[1]Corresponding author.

Contributed by the Manufacturing Engineering Division of ASME for publication in the Journal of Micro- and Nano-Manufacturing. Manuscript received March 25, 2017; final manuscript received November 1, 2017; published online December 14, 2017. Assoc. Editor: Takashi Matsumura.

to avoid cracks, bubbles, and fluid instability of the core material(s).

(5) The cladding and core materials should have relatively compatible thermal expansion coefficients in the temperature range up to the drawing temperature.

Following the previous criteria, however, does not guarantee the continuity of the metal core. Establishment of process parameters relies mostly on experiences and often involves trial-and-error.

Low melting temperature metals such as tin (Sn), bismuth (Bi), indium (In), and their alloys have been thermally drawn in polymer cladding, such as polyethersulfone (PES), polysulfone, and polyethylenimine with a softening temperature below 300 °C. The resulting metal fibers with rectangular or circular cross sections have critical dimensions ranging from tens to hundreds of micrometers. They are also thermally drawn along with other functional materials (usually semiconductors or conductive polymers) and serve as conductive electrodes in multimaterial functional fibers, which are in turn utilized as one-dimensional photodetectors [4], thermal sensors [5,6], piezoelectric transducers [7,8], chemical sensors [9], and capacitors [10]. The smallest diameter reported for metal wires that can be reliably drawn into infinitely long filaments is about 4 μm and was achieved from $Sn_{0.95}Ag_{0.05}$ alloy with PES cladding [11]. Beads, discontinuities, and structural deformation would be observed upon further size reduction. Nevertheless, thermally drawn functional fibers embedding indium wires with diameter approaching 1 μm have been demonstrated [12]. Indium arrays were thermally drawn in polymethyl methacrylate cladding to yield a metamaterial fiber that exhibits electric and magnetic responses for terahertz and far-infrared spectrum.

Despite the fact that reliable drawing of indefinitely long amorphous semiconductor and polymer nanowires has been achieved [11], literature survey above suggests that there exists a fundamental size limit to the diameter of thermally drawn crystalline metal wires below which the metal wires become inherently unstable and extremely difficult to control, if not impossible, by current manufacturing techniques. The physical forces that dominate the break-up, however, are still in dispute. Some attribute the break-up to Plateau-Rayleigh instability [13] while others suggest metal cannot withstand shear stress [11]. Resolution of this challenge meets roadblocks both theoretically and experimentally. No model can yet satisfactorily describe the dynamics of the molten metal core during preform fiber drawing, as pointed out by Zhao et al. [14], although numerous works concerning the modeling and simulation of the compound and microstructured fiber drawing processes exist [15–18]. Recent attempt made is based on Tomotika's model that was established nearly a century ago [13,19], which considered the break-up of a cylindrical thread in a surrounding flow that is extending uniformly. Quantitative comparisons between simulation and experiments are emerging [20,21], yet far from being applicable for real-time control. Experimental investigation of the core dynamics, on the other hand, is equally challenging, which require high-speed, high-resolution characterization of high aspect-ratio objects embedded in a thick glass/polymer material under high temperature. A simple yet useful model is called for to elucidate the underlying mechanism of diameter control and to predict in real-time the core continuity from measurable process parameters and material properties.

In addition to its implication in manufacturing of continuous metal microwires, the model also leads us to believe that metal core fiber drawing from a preform may provide a new way for study and control of fluid interfaces in addition to the existing flow fields such as entrainment problems [22], flow focusing [23], and microfluidic devices [24]. With the various studies pointing out the possibility of obtaining nanoscale droplets by hydrodynamic forces [14], further advancement of knowledge is hindered by the lack of methods for experimental observation and in-line metrology. The fact that the shape of the metal wires is formed at liquid state while can be observed at solid state provides an unexpected yet new way for the study of the complex nonlinear dynamics of fluid flows at micro/nanoscales.

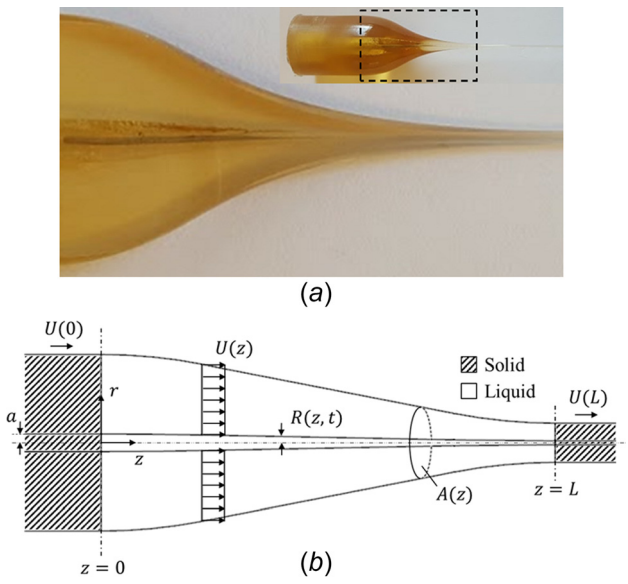

Fig. 2 Image of the neck-down region (*a*) and the schematic (*b*) corresponding to an axisymmetric free surface extensional flow in the cladding entraining an immiscible molten metal from a nozzle (or melt front) located at $z = 0$. The entrained molten metal core has radius $R(z, t)$. Downstream at $z = L$, the metal solidifies with diameter $R(L, t)$.

Problem Formulation

During a typical thermal drawing process, as the preform is slowly fed into the furnace at a constant speed and uniform fibers being pulled from below as shown in Fig. 1, a steady-state in Eulerian frame is soon reached such that the temperature and velocity of the cladding vary along the axis of symmetry but do not change with time, if viewed from a fixed laboratory position. We focus on the dynamics of the molten metal core under the condition that the cladding flow is steady, requiring that the diameter of cladding is much larger than the core $A(z) \gg \pi R^2(z, t)$ so that the molten metal core is assumed to have negligible effect on the cladding flow except for the region in the vicinity of the centerline (Fig. 2).

We consider preform drawing of Sn microwire in Pyrex cladding. For the exterior cladding flow, inertia, gravity, and surface tension are assumed to be negligible as compared to the viscous term in the cladding flow following Yarin et al. [25]. For the interior metal flow, the corresponding values of the Reynolds, Weber, and Bond numbers of the molten core under the parameters given in Table 1 are calculated as follows: $\mathrm{Re} = (2\rho\bar{U}\bar{R}/\mu_0) = 0.4$, $\mathrm{We} = (2\rho\bar{U}^2\bar{R}/\gamma) = 2 \times 10^{-5}$, $\mathrm{Bo} = (4\Delta\rho g a^2/\gamma) = 9 \times 10^{-4}$, all of which are much smaller than 1, allowing us to neglect the core inertia and gravity effects. The length of the thread length is the length of the neck-down region measured on the drawn preform from the point where its diameter starts to shrink to the point where the shrinkage ceases.

Effect of the thermal gradient requires further consideration. The viscosity of the cladding is very sensitive to temperature and undergoes orders of magnitude variations along the thread line, and thus cannot be neglected. Viscosity change of the molten metal core due to thermal gradient is neglected since $\mu_0 \ll \mu(z)$. Thermal gradient also introduces interfacial tension gradient along the thread line, which may result in Marangoni flow that can be approximated by

$$-\frac{d\gamma}{dT}\frac{dT}{dz} = \mu\frac{\partial u_z}{\partial r} \tag{1}$$

where u_z is the surface velocity due to Marangoni flow in the axial direction, assuming a cylindrical interface. A dimensionless number can therefore be defined to gauge the strength of the Marangoni flow $\text{Ma} = -(d\gamma/dT)(4\Delta T\bar{R}/\mu\bar{U}L) = 1.64 \times 10^{-8} 1.64 \times 10^{-8}$ compared to the cladding flow, which in this case is small, allowing us to neglect the Marangoni flow induced by thermal gradient.

The steady-state cladding flow without core is modeled as a quasi-one-dimensional free surface extensional flow with velocity $(-(r/2)(dU(z)/dz), 0, U(z))$. We let molten metal of viscosity μ_0 be entrained from a nozzle or melt front with radius a by the extensional cladding flow with position dependent viscosity $\mu(z)$, and solidifies downstream at $z = L$ with radius $R(L,t)$. Focusing on the limit $\mu_0 \ll \mu(z)$ following Taylor, Acrivos, Sherwood, and others' works [30–32], the coupling between the interior metal flow and the exterior cladding flow simplifies to a balance between the interior pressure and the exterior stress, and the entrainment dynamics can be accurately described by a long-wavelength model provided that the slope of the spout is everywhere small.

Extruded polyethersulfone (PES, BASF Ultrason E3010) rods (extruded and distributed by Port Plastics, Inc.) with an outer diameter of 19.05 mm and length of 10 cm were first dehydrated at 150 °C for 5 days under vacuum (2 Torr) to remove moisture. A through hole was then drilled to allow insertion of a Sn metal wire (SRA Soldering Products, Foxborough, MA). The PES preform was then slowly fed into a vertical tube furnace at 250 °C at a speed of 50 μm/s under a vacuum of 40 mTorr to consolidate the preform and ensure seamless contact between the metal core and the cladding. The consolidated preform was used either for thermal drawing or interfacial energy measurement.

Unsteady volume conservation inside the spout gives

$$\frac{\pi\partial R^2(z,t)}{\partial t} + \frac{\partial Q(z,t)}{\partial z} = 0 \tag{2}$$

where $Q(z,t)$ is the flow rate of core.

The velocity inside the molten metal core is nearly unidirectional and is composed of a plug flow induced by the cladding flow and a pressure driven flow, which has the form

$$\mathbf{u}_{\text{core}} = u(z,r,t)\mathbf{e}_z = \left[U(z) - \frac{1}{4\mu_0}\frac{\partial P_0(z,t)}{\partial z}\left(R^2(z,t) - r^2\right)\right]\mathbf{e}_z \tag{3}$$

where $P_0(z,t)$ is the interior pressure, and $R(z,t)$ is the radius of the metal core.

At $z = 0$, the molten metal comes out from the melt front or a nozzle connected to a large reservoir, so the pressure in the metal is determined by the local stress at the core/cladding interface. We thus obtain an expression for $P_0(z,t)$

$$P_0(z,t) = 2\mu(z)\left(\frac{dU(z)}{dz} + \frac{1}{R(z,t)}\frac{\partial R(z,t)}{\partial t} + \frac{U(z)}{R(z,t)}\frac{\partial R(z,t)}{\partial z}\right) + P_{\text{clad}}(r,z) + \gamma\kappa \tag{4}$$

which contains contributions from surface tension due to the full curvature $\kappa = 1/R(z,t)(1 + (\partial R(z,t)/\partial z)^2)^{\frac{1}{2}} - \partial^2 R(z,t)/\partial z^2 /(1+ (\partial R (z,t)/\partial z)^2)^{\frac{3}{2}} \approx 1/R(z,t) - \partial^2 R(z,t)\partial z^2$ pressure and viscous stress in the cladding.

Flow rate of core is therefore

$$\begin{aligned} Q(z,t) &= \int_s u(z,r,t)dS = 2\pi\left[\frac{U(z)R^2(z,t)}{2} - \frac{R^4(z)}{16\mu_0}\frac{d}{dz}P_0(z,t)\right] \\ &= \pi U(z)R^2(z,t) - \frac{\pi R^4(z,t)}{8\mu_0} \\ &\quad \times \left\{\frac{\partial}{\partial z}\left[3\mu(z)\left(\frac{dU(z)}{dz} + \frac{2}{3R(z,t)}\frac{\partial R(z,t)}{\partial t}\right.\right.\right. \\ &\quad \left.\left.\left. + \frac{2U(z)}{3R(z,t)}\frac{\partial R(z,t)}{\partial z}\right) + \gamma\kappa\right] + \frac{d\mu(z)}{dz}\frac{dU(z)}{dz}\right\} \end{aligned} \tag{5}$$

where $u(z,r,t)$ is the core velocity, $S(z,t)$ the cross-sectional area of the core.

The unknown quasi-one-dimensional velocity field can be obtained by volume conservation to give $U(z) = A(0)U(0)/A(z)$, where the cross-sectional area of the cladding $A(z)$ can be easily measured. The unknown position-dependent viscosity can be approximated by $\mu(z) = -(A(z)F/3A(0)U(0))(dA(z)/dz)^{-1}$ [33], knowing draw force $F = 3A(z)\mu(z)(dU(z)/dz)$.

Plugging Eq. (5) into Eq. (2) yields a fourth-order nonlinear differential equation to be solved given $A(z)$ and F, both being measurable. While previous works focus on the zero flow rate limit $Q(0,t) \to 0$ in a linear straining flow [22] or pressure driven flow [34,35], this work focuses on $Q(0,t) = \pi a^2 U(0)$ in a nonlinear free surface extensional flow with position-dependent viscosity.

Boundary Conditions and Diameter Control Mechanism

At the nozzle opening or melt front under steady-state drawing, the flow rate of molten metal is controlled at $Q(0,t) = Q_{\text{core}}$. Downstream, due to the fact that the solidified metal core has same velocity as the cladding assuming no slip between solidified

Table 1 Material properties and process parameters

Parameters	Symbol	Approximate value	Units
Density of PES melt [26]	ρ_{PES}	1212.6	kg m^{-3}
Density of molten Sn at melting point [27]	ρ_{Sn}	6990	kg m^{-3}
Sn/PES interfacial energy	γ	0.319	J m^{-2}
Temperature dependency of interfacial energy [28]	$d\gamma/dT$	−0.1	mJ m^{-2} K^{-1}
Length of thread line	L	4.129	cm
Feeding speed	$U(0)$	20	μm s^{-1}
Pulling speed	$U(L)$	10	mm s^{-1}
Average speed	$\bar{U}$	5	mm s^{-1}
Viscosity of core [29]	μ_0	0.003	Pa·s
Initial core radius	a	35.7	μm
Average core radius	$\bar{R}$	17.85	μm
Tensile stress at $z = L$	T_{zz}	1.65	MPa
Temperature rise above melting point of metal	ΔT	∼100	K
Viscosity of cladding under isothermal condition	μ	2.115×10^5	Pa·s

Table 2 Process parameters for experimental validation of the diameter control mechanism

Run	Q_{core}(m^3/s)	$U(0)$(m/s)	$U(L)$(m/s)	$\sqrt{\frac{Q_{core}}{\pi U(L)}}$ (m)	$R(L)$ (m)	Std. dev. (m)
1	1.74×10^{-13}	1×10^{-5}	1.41×10^{-3}	6.27×10^{-6}	6.82×10^{-6}	5×10^{-7}
2	1.61×10^{-11}	8×10^{-6}	1×10^{-2}	2.26×10^{-5}	2.43×10^{-5}	1×10^{-6}
3	2.01×10^{-11}	1×10^{-5}	1.41×10^{-3}	6.74×10^{-5}	6.79×10^{-5}	8×10^{-6}

core and cladding, the radius of the solidified metal $R(L,t)$ is therefore determined by the drawing speed $U(L)$ of the cladding and the flow rate $Q(L,t)$ of molten metal at the solidification front to give $R(L,t) = \sqrt{Q(L,t)/\pi U(L)}$, neglecting the density change of the metal due to solidification. These constitute the boundary conditions $R(0,t) = a$, $Q(0,t) = Q_{core}$, and $R(L,t) = \sqrt{Q(L,t)/\pi U(L)}$.

Under a steady-state drawing, metal wire produced being continuous and uniform requires the flow rate of metal core at the solidification front to be independent of time; thus, $Q(L,t) = Q(L)$. Volume conservation inside the metal jet further requires that the amount of molten metal enters at $z = 0$ equals to the amount exits at $z = L$, yielding $Q(L) = Q(0) = Q_{core}$. The third boundary condition $R(L,t) = \sqrt{Q(L,t)/\pi U(L)}$ is thus turned into $R(L) = \sqrt{Q_{core}/\pi U(L)}$ under steady-state drawing. Recognizing that $Q_{core} = \pi a^2 U(0)$ for preform drawing, and plugging in the third boundary condition to give $R(L) = a\sqrt{U(0)/U(L)} = a\sqrt{1/D_r}$, we have shown that the diameter control mechanism for continuous metal microwire production by preform drawing is essentially volume conservation and the metal core diameter does follow the draw-down ratio, if a steady-state can be reached.

To validate the proposed diameter control mechanism, steady-state drawings were done under the parameters listed in Table 2 and cross sections of the resultant metal core fibers are shown in Fig. 3. A linear fit of $R(L)$ with $\sqrt{Q_{core}/\pi U(L)}$ is plotted in Fig. 4. The slope is 0.9945 with the coefficient of determination equals to 0.9996, suggesting $R(L) = \sqrt{Q_{core}/\pi U(L)}$. We can thus conclude that the diameter of the metal produced indeed follow draw down ratio Dr $= (U(L)/U(0))$, provided that the flow rate is controlled at the nozzle or melt front so that the feeding speed of the metal is the same as the feeding speed of the cladding, a diameter control mechanism that potentially holds valid down to nanoscale in principle but never explicitly stated in the literature. It should be noted that the variation in the value of the vertical axis in Fig. 4 can be attributed to the growth of capillary instability on the metal core during drawing. A cylindrical molten metal thread is inherently unstable due to its high surface tension. A sinusoidal wave therefore grows spontaneously giving rise to the variation of the diameter of the metal core along the thread line. Since the magnitude of the growth of the capillary instability is proportional to the base diameter, the variation of the core diameter appears larger for larger cores. In some cases, the growth of capillary instability would eventually disrupt this assumption and result in slopes not equal to one, which lead us to use this as a criteria to test core continuity. In other words, the slope shall always be equal to one as long as the metal core is continuous.

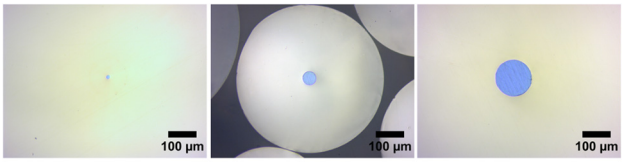

Fig. 3 Cross-sectional images of the metal core fibers obtained from process parameters given in Table 2

Steady-State Core Shape

(i) Isothermal drawing with constant cladding velocity and zero core flow rate ($\boldsymbol{U}(z) = \boldsymbol{U}(0)$, $\boldsymbol{\mu}(z) = \boldsymbol{\mu}$, $\boldsymbol{Q}(z,t) = 0$)
In the simplest case, when $U(z) = U(0)$, $\mu(z) = \mu$, and $Q(z,t) = 0$, Eq. (5) is reduced to

$$Q(z,t) = \pi U(0) R^2(z,t) - \frac{\pi R^4(z)}{8\mu_0} \left\{ \frac{d}{dz}\left[2\mu \left(\frac{1}{R(z,t)} \frac{\partial R(z,t)}{\partial t} + \frac{U(0)}{R(z,t)} \frac{\partial R(z,t)}{\partial z} \right) + \frac{\gamma}{R(z,t)} - \frac{\gamma d^2 R(z,t)}{dz^2} \right] \right\} \tag{6}$$

Rescaling all radial length scales by a, axial length scales by $a\sqrt{\mu/4\mu_0}$, pressure by (γ/a), and solve for steady-state solution, we obtain

$$R^*(z^*) = \frac{-\frac{1}{U^*} \pm \sqrt{\left(\frac{1}{U^*}\right)^2 - 4}}{2} z^* + 1 \tag{7}$$

where $U^* = (4\sqrt{\mu\mu_0} U_0/\gamma)$. We have thus shown that our model includes the conical fluid interface solution first derived by Taylor [36] as a special case.

(ii) Isothermal drawing with exponential cladding velocity

$$\left(\boldsymbol{U}(z) = \boldsymbol{U}(0) \left(\frac{\boldsymbol{U}(\boldsymbol{L})}{\boldsymbol{U}(0)} \right)^{\frac{z}{L}}, \boldsymbol{\mu}(z) = \boldsymbol{\mu} \right)$$

The cladding profile is available in an exponential form for isothermal drawing of Newtonian fluid [37] with $U(z) = U(0)(U(L)/U(0))^{z/L}$. In Fig. 5, the analytical cladding profile is plotted against the actual cladding profile drawn under the conditions listed in Table 1.

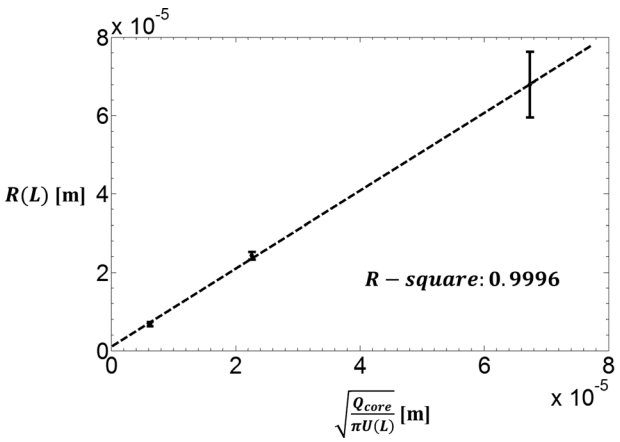

Fig. 4 Experimental result supporting the proposed diameter control mechanism

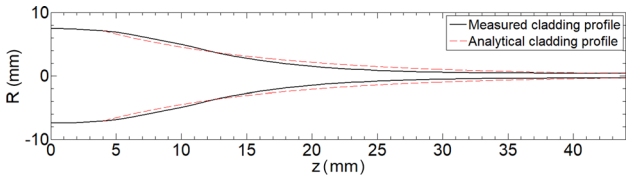

Fig. 5 Measured and analytical cladding profile

Plugging the analytical profile into Eq. (5) assuming both cladding and core are at steady-state, and neglecting axial pressure gradient in the cladding we obtain the expression for the flow rate

$$Q = 2\pi\left\{\frac{U_0 D_r^{\frac{z}{L}} R^2(z)}{2} - \frac{R^4(z)}{16\mu_0}\frac{d}{dz} \times\left[2\mu U_0 D_r^{\frac{z}{L}}\left(\frac{\ln D_r}{L} + \frac{1}{R(z)}\frac{dR(z)}{dz}\right) + \gamma\left(\frac{1}{R(z)} - \frac{d^2R(z)}{dz^2}\right)\right]\right\} \tag{8}$$

If we scale z by L, R by a, and Q by $\pi a^2 U(0)$, we obtain Eq. (8) in the dimensionless form

$$Q^*U^* = U^* D_r^{z^*} R^{*2}(z^*) - R^{*4}(z^*)\frac{d}{dz^*} \left[\mathrm{Ca} D_r^{z^*}\left(1 + \frac{1}{\ln D_r}\frac{1}{R^*(z^*)}\frac{dR^*(z^*)}{dz^*}\right) + \frac{1}{R^*(z)} - \frac{1}{AR^2}\frac{d^2R^*(z)}{dz^{*2}}\right] \tag{9}$$

where $\mathrm{Ca} = 2a\mu U_0 \ln D_r/\gamma L$ is the dimensionless strain rate at the nozzle opening; $U^* = 4\lambda AR^2 \mathrm{Ca}/\ln D_r$, where $\lambda = (\mu_0/\mu)$, $\mathrm{AR} = (L/a)$;Q^* is the dimensionless flow rate of metal with $Q^* = 1$ meaning metal is flowing at the same average velocity as the cladding at the melt front. This scaling allows the domain of z^* be fixed as $[0, 1]$ with $R^*(0) = 1$ and $R^*(1) = \sqrt{Q^*/D_r}$.

Numerical solution of Eq. (9) is obtained using bvp4c function in MATLAB with parameters listed in Table 1, under a third boundary condition

$$\left.\frac{dR^*(z^*)}{dz^*}\right|_{z^*=1} = 0$$

The shape of the entrance and exit areas matches the theoretical calculations very well. However, the shape of the calculated metal core during steady-state drawing appears similar to the "die swelling" phenomenon due to the viscoelasticity of the polymer melt typically encountered in melt spinning of polymeric fibers. Here, our theory predicts that "die swelling" may also occur during preform drawing of a Newtonian molten metal within a Newtonian cladding as shown in Fig. 6. Yet such swelling behavior is not observed in the measured core profile, possibly because the calculation was based on isothermal cladding profile while the actual profile is obtained under nonisothermal drawing. Multiple tasks are planned as future works to reduce the discrepancy between experimental and theoretical data. The isothermal cladding profile would first be replaced by the actual cladding profile for the calculation of the core profile to take into account the effect of temperature gradient in the axial direction. Other sources of errors would be screened as well. The validity of the quasi-one-dimensional assumption for the cladding flow would be tested by numerical simulations of the two-dimensional cladding flow taking into account both momentum and energy transport. The measurement method would be improved by installing a high-speed camera to the drawing tower to capture the cladding profile in real time to eliminate the errors introduced by solidification of the cladding and core. Measurements and calculations would be conducted on other material pairs such as glass/metal combinations to eliminate the non-Newtonian effect of the polymer cladding. The ultimate goal is to obtain a valid model that can be used for the feedback control of process parameters during the continuous and reliable production of metal core fibers.

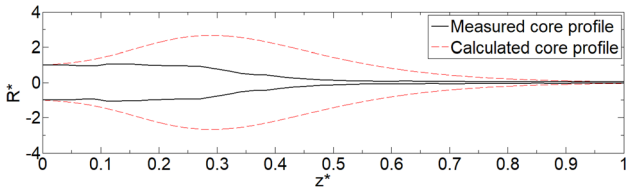

Fig. 6 Measured and calculated core profile

Measurement of Interfacial Energy

In the previous calculation, the data of interfacial energy between PES and Sn were needed. However, interfacial energy data for liquid–liquid interfaces between metals and polymers are almost nonexistence in the literature. There are increasing needs [13] for such data for the manufacturing of metal micro/nanowires as well as functional multimaterial fibers. Here, the interfacial energy γ between the molten Sn and PES was measured by sessile drop method using the following equation derived by Birdi et al. [38]:

$$\gamma = \frac{\Delta\rho g H^2}{2(1-\cos\theta)} \tag{10}$$

where $\Delta\rho$ is the density difference between the drop and its surrounding, g is the gravitational force of acceleration, H is the limiting drop height, and θ is the contact angle.

To minimize oxidation of the molten metal at high temperature, a dripping method was designed and employed as shown in Fig. 7 to avoid exposure of molten metal to ambient air. A consolidated preform was subjected to furnace heating at 350 °C with an alumina crucible placed below. The lower portion of the preform softened and dripped down into the crucible. A single drop of molten Sn surrounded by PES was thus obtained.

Eight droplets with increasing volume were made, whose drop heights are plotted against their volume to make sure that the height of the largest droplets does reach the limiting height H as shown in Fig. 8. Droplets with heights within 5% of the limiting height are used for the measurement of the interfacial energy.

Measurement of contact angles and drop heights was done on the images of the solidified droplet, which is routinely applied for the estimation of surface tension of molten metals [28]. Figure 9 shows optical images of the Sn droplet after removal of the PES by dissolving in Dichloromethane for contact angle measurement.

Images for three droplets were taken using APPR® B/W digital camera and First Ten Angstroms video software. Drop heights

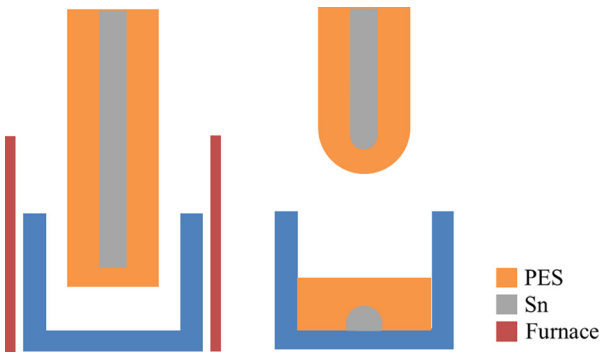

Fig. 7 Schematic of the procedure to obtain a Sn sessile drop surrounded by PES

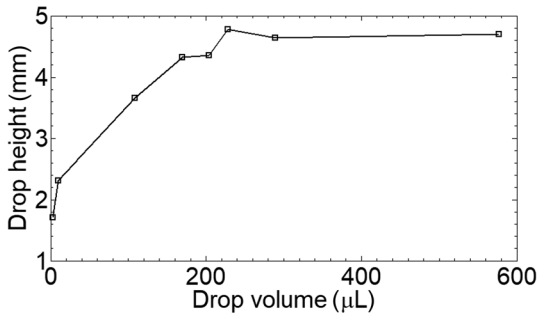

Fig. 8 Drop height versus drop volume

Fig. 9 A solidified Sn droplet after removing the PES for contact angle measurements

Table 3 Interfacial energy measurement

No.	θ (deg)	H (mm)	$\Delta\rho$ (kg/m^3)	g (m/s^2)	γ (J/m^2)
1	163.2	4.7	5777.4	9.8	0.319
2	164.9	4.78	5777.4	9.8	0.329
3	165.5	4.64	5777.4	9.8	0.309

were measured by a caliper, and contact angles were measured by ImageJ [39] with the drop shape analysis plugin developed by Stalder et al. [40].

Measurement results are summarized in Table 3. The interfacial energy between Sn and PES at around the melting point of Sn was determined to be 0.319 ± 0.010 J/m^2, which was listed in Table 1 earlier.

Mode Transition and Critical Capillary Number

We suggest a dimensionless capillary number $\mathrm{Ca} = 2Fa/\gamma A(0)$ to be used as the indicator of the mode transition from continuous entrainment (i.e., viscous stress dominating) to capillary break-up (interfacial tension dominating). The capillary number is defined as the ratio between the stress in the cladding at the melt front $F/A(0)$ and the Laplace pressure due to the interfacial tension

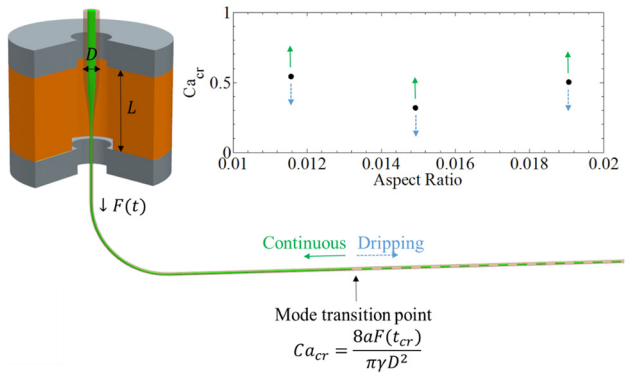

Fig. 10 Capillary number versus aspect ratio

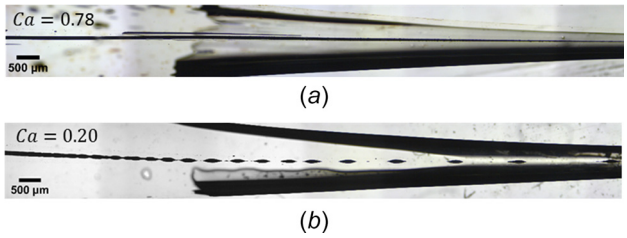

Fig. 11 Continuous mode (*a*) and dripping mode (*b*)

$(\gamma/2a)$, where F is the drawing force, $A(0)$ is the diameter of the preform, γ is the interfacial tension, and a is the initial radius of the metal core. Interfacial tension leads to capillary break-up while viscous stress in the cladding acts against it. Ca therefore measures the likelihood of the core breaking due to interfacial tension. Large Ca ($\mathrm{Ca} > 1$) suggests viscous stress is dominating resulting in the growth of capillary instability being suppressed. Small Ca ($\mathrm{Ca} < 1$) suggests interfacial tension dominating; thus, the metal core has higher chance to disintegrate. A continuous core may start to break as capillary number reduces below a critical value. And a discontinuous core may start to become continuous as the capillary number increases. It can be expected that a critical capillary number Ca_{cr} exists, which marks the mode transition. Experiments were conducted to measure the critical capillary number as shown in Fig. 10, and the results were plotted against the aspect ratio, which is the ratio between the cladding diameter and the furnace length. For each data point, a metal core preform is continuously drawn with drawing force measured and recorded as the furnace temperature is slowly reduced. Great care was taken to ensure that the mode transition occurred during each run. The exact location where the mode transition occurred is found under a microscope by examining the drawn fibers. The critical time t_{cr} that the mode transition occurred is determined by dividing the length of the drawn fibers by the drawing speed. The value of the drawing force at t_{cr} can then be determined from the recorded data. The critical capillary number appears to be on the order of 0.5 in the range of aspect ratio studied.

Optical micrographs of the core continuity under continuous mode drawing and dripping mode drawing are shown in Fig. 11. Below Ca_{cr}, the metal core breaks due to capillary instability and forms a train of stretched droplets that translate downstream as they are deformed in the cladding flow when $\mathrm{Ca} = 0.20$ as shown in Fig. 11(*b*), while Fig. 11(*a*) shows the optical micrograph of a solidified metal core that is continuous and drawn under a capillary number $\mathrm{Ca} = 0.78$. The critical capillary number, in this case, falls between 0.2 and 0.78.

Conclusions

We have extended previous authors' theoretical work on viscously entrained jet dynamics and derived a long wavelength model that may be used to solve for the dynamics of the molten metal core during the production of continuous metal microwires by thermal fiber drawing from a preform. Examination of the boundary conditions revealed that the diameter control mechanism for continuous microwire production by preform drawing is essentially volume conservation. The flow rate of molten metal is controlled upstream while the flow velocity is controlled downstream realized by solidification of the molten metal. This mechanism works for the diameter control of nanowire in principle as well. Scaling analysis revealed that the dominant physical forces that govern the dynamics of the metal jet are interfacial tension, stress in the cladding, and pressure in the metal. The accuracy of the model can be improved by replacing the cladding flow with a more accurate profile, either obtained analytically [33], by simulation [41] or measurements [42]. Although derived for metal drawing, semiconductor core is applicable as well, as long as it is molten during drawing. Steady-state solution of the model is

compared with experiments and discrepancies attributed to the fact that the process is nonisothermal. A general and simple method to measure the liquid–liquid interfacial energy between molten metal and viscous claddings was designed and implemented for Sn/PES interface. A dimensionless capillary number $\mathrm{Ca} = 2Fa/\gamma A(0)$ is suggested to be used as the indicator for the transition from continuous mode (i.e., viscous stress dominating) to dripping mode (i.e., interfacial tension dominating). Experiments suggest the existence of a critical capillary number above which continuous metal microwires can be produced, providing the first ever quantitative measure of the core continuity during preform drawing of metal microwires based on process parameters and material properties.

Acknowledgment

The authors are grateful to Yu-sheng Kuo, Shenzhen Xu, Zhengxian Qu, Elaheh Alizadehbirjandi, Maher Lagha, Pirouz Kavehpour, and Gan-ce Dai for insightful suggestions.

Funding Data

- National Science Foundation (Grant No. 1449395).

Nomenclature

$A(z)$ = preform diameter at z
Ca = capillary number
$\mathrm{Ca_{cr}}$ = critical capillary number
D_f = fiber diameter
D_p = preform diameter
D_r = draw down ratio
F = drawing force
H = limiting droplet height
L = thread length
Q = flow rate
$R(z,t)$ = core radius at position z at time t
T_g = glass transition point of cladding
T_m = melting point of metal core
T_{zz} = axial stress
$U(0)$ = feeding speed
$U(L)$ = pulling speed
γ = interfacial energy between core and cladding
θ = contact angle
μ = viscosity of cladding
μ_0 = viscosity of core
ρ = density

Appendix: Detailed Derivation

The steady-state cladding flow without core is modeled as a quasi-one-dimensional free surface extensional flow with velocity $(-(r/2)(dU(z)/dz), 0, U(z))$, where $U(z) = (A(0)U(0)/A(z))$ by mass conservation and $A(z)$ is the cross-sectional area of the cladding. We let molten metal of viscosity μ_0 be entrained from a nozzle or melt front with radius a by the extensional cladding flow with position-dependent viscosity $\mu(z)$, and solidifies downstream at $z = L$ with radius $R(L,t)$. Focusing on the limit $\mu_0 \ll \mu(z)$ following Taylor, Acrivos, Sherwood, and others' work [30–32], the coupling between the interior flow and the exterior flow simplifies to a balance between the interior pressure and the exterior stress, and the entrainment dynamics can be accurately described by a long-wavelength model provided that the slope of the spout is everywhere small.

Since $\mu_0 \ll \mu$ and the molten metal core are long and slender, we follow Taylor [31], Zhang [22], and Gordillo et al. [35] in modeling the effect of molten metal core on the cladding flow as a radial flow, $(q(z,t)/2\pi r)$, corresponding to a line of point sources of unknown intensities situated along z-axis. The velocity field in the vicinity of the molten metal core has the form

$$\left(-\frac{r}{2}\frac{dU(z)}{dz}, 0, U(z)\right) + \left(\frac{q(z,t)}{2\pi r}, 0, 0\right) \tag{A1}$$

where $q(z,t)$ is the strength of the volume flux and has to be determined by the kinematic boundary conditions on the core/cladding interface. The velocity inside the molten metal core is nearly unidirectional and is composed of a plug flow induced by the exterior flow and a pressure-driven flow, which has the form

$$\mathbf{u}_{\mathrm{core}} = u(z,r,t)\mathbf{e}_z = \left[U(z) - \frac{1}{4\mu_0}\frac{\partial P_0(z,t)}{\partial z}\left(R^2(z,t) - r^2\right)\right]\mathbf{e}_z \tag{A2}$$

where $P_0(z,t)$ is the interior pressure, and $R(z,t)$ is the radius of the metal core.

The kinematic boundary condition on the core/cladding interface is $(\partial R(z,t)/\partial t) + \mathbf{u}_{\mathrm{clad}} \cdot \mathbf{n}|_{r=R(z,t)} = 0$. Making use of the fact that the core is long and slender, we have at leading order $\mathbf{n}|_{r=R(z,t)} = (-1, 0, \partial R(z,t)/\partial z)$. This kinematic boundary condition together with Eq. (A1) yields an expression for the line flux

$$\frac{q(z,t)}{2\pi r}|_{r=R(z,t)} = \frac{\partial R(z,t)}{\partial t} + U(z)\frac{\partial R(z,t)}{\partial z} + \frac{1}{2}R(z,t)\frac{dU(z)}{dz} \tag{A3}$$

The normal stress balance across the spout interface has the form

$$\sigma_{rr}^{\mathrm{ext}} - \gamma\kappa = \sigma_{rr}^{\mathrm{int}} \tag{A4}$$

where κ is the curvature of the interface, γ is the interfacial energy of the interface, $\sigma_{rr}^{\mathrm{ext}}$ is the normal stress contribution from flow outside the core, and $\sigma_{rr}^{\mathrm{int}}$ is the normal stress contribution from flow inside the core. The exterior normal stress contribution evaluated at the interface is

$$\begin{aligned}\sigma_{rr}^{\mathrm{ext}}|_{r=R(z)} &= -P_{\mathrm{clad}}(r,z) + 2\mu\frac{\partial u_r(r,z)}{\partial r}|_{r=R(z)} \\ &= -P_{\mathrm{clad}}(r,z) - 2\mu(z) \\ &\quad\times\left(\frac{dU(z)}{dz} + \frac{1}{R(z,t)}\frac{\partial R(z,t)}{\partial t} + \frac{U(z)}{R(z,t)}\frac{\partial R(z,t)}{\partial z}\right)\end{aligned} \tag{A5}$$

where we have taken the pressure at infinity to be 0. The pressure gradient in the axial direction due to the cladding flow without the line source is

$$\frac{\partial P_{\mathrm{clad}}(r,z)|_{r=R(z)}}{\partial z} = \mu(z)\frac{d^2U(z)}{dz^2} + 2\frac{\partial\mu(z)}{\partial z}\frac{\partial U(z)}{\partial z}$$

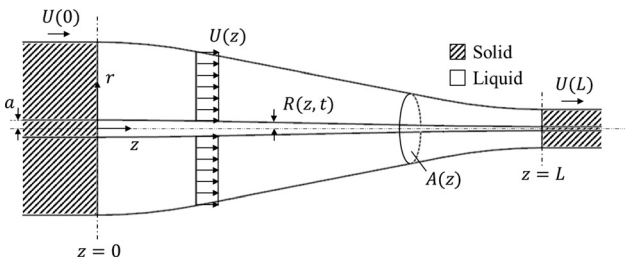

Fig. 12 An axisymmetric free surface extensional flow $(-(r/2)(dU(z)/dz), 0, U(z))$ in the cladding entrains an immiscible molten metal from a nozzle (or melt front) located at $z = 0$. The entrained molten metal core has radius $R(z,t)$. Downstream at $z = L$, the metal solidifies with diameter $R(L,t)$.

from momentum conservation. The pressure gradient due to the line source is neglected following Gordillo et al. [35] since $\nabla P_{\text{source}} = 0$ in the zero-Reynolds-number limit.

In contrast, the interior normal stress contribution is dominated by the interior pressure P_0, which can be seen by combining Eq. (A2) with the continuity equation and solve for the deviatoric stress contribution to σ_{rr}^{int}

$$2\mu_0 \frac{\partial u_r(r,z)}{\partial r} = 2\mu_0 \frac{dU(z)}{dz} + \frac{1}{2}\frac{\partial^2 P_0(z)}{\partial z^2}\left(R(z)^2 - r^2\right) + R(z)\frac{dR(z)}{dz}\frac{\partial P_0(z)}{\partial z} \tag{A6}$$

in which all contributions are small relative to P_0.

At $z = 0$, the molten metal comes out from the melt front or a nozzle connected to a large reservoir, so the pressure in the metal is determined by the local stress at the core/cladding interface. We thus obtain an expression for $P_0(z,t)$

$$P_0(z,t) = 2\mu(z)\left(\frac{dU(z)}{dz} + \frac{1}{R(z,t)}\frac{\partial R(z,t)}{\partial t} + \frac{U(z)}{R(z,t)}\frac{\partial R(z,t)}{\partial z}\right) + P_{\text{clad}}(r,z) + \gamma\kappa \tag{A7}$$

which contains contributions from surface tension due to the full curvature

$$\kappa = \frac{1}{R(z,t)\left(1+\left(\frac{\partial R(z,t)}{\partial z}\right)^2\right)^{\frac{1}{2}}} - \frac{\frac{\partial^2 R(z,t)}{\partial z^2}}{\left(1+\left(\frac{\partial R(z,t)}{\partial z}\right)^2\right)^{\frac{3}{2}}} \approx \frac{1}{R(z,t)} - \frac{\partial^2 R(z,t)}{\partial z^2}$$

pressure and viscous stress in the cladding. Unsteady volume conservation inside the spout gives

$$\frac{\pi\partial R^2(z,t)}{\partial t} + \frac{\partial Q(z,t)}{\partial z} = 0 \tag{A8}$$

where $Q(z,t)$ is the flow rate of core

$$\begin{aligned} Q(z,t) &= \int_s u(z,r,t)dS = 2\pi\left[\frac{U(z)R^2(z,t)}{2} - \frac{R^4(z)}{16\mu_0}\frac{d}{dz}P_0(z,t)\right] \\ &= \pi U(z)R^2(z,t) - \frac{\pi R^4(z,t)}{8\mu_0} \\ &\times \left\{\frac{\partial}{\partial z}\left[3\mu(z)\left(\frac{dU(z)}{dz} + \frac{2}{3R(z,t)}\frac{\partial R(z,t)}{\partial t} + \frac{2U(z)}{3R(z,t)}\frac{\partial R(z,t)}{\partial z}\right) + \gamma\kappa\right] + \frac{d\mu(z)}{dz}\frac{dU(z)}{dz}\right\} \end{aligned} \tag{A9}$$

where $u(z,r,t)$ is the core velocity, $S(z,t)$ is the cross-sectional area of the core

$$U(z) = \frac{A(0)U(0)}{A(z)},\ \mu(z) = -\frac{A(z)F}{3A(0)U(0)}\left(\frac{dA(z)}{dz}\right)^{-1}$$

and F the drawing force derived from the tensile stress

$$\frac{F}{A(z)} = 3\mu(z)\frac{dU(z)}{dz}$$

References

[1] Tao, G., Stolyarov, A. M., and Abouraddy, A. F., 2012, "Multimaterial Fibers," Int. J. Appl. Glass Sci., **3**(4), pp. 349–368.

[2] Ma, Z., Hong, Y., Ding, S., Zhang, M., Hossain, M., and Su, M., 2011, "Three-Dimensional Micro/Nanomaterials Generated by Fiber-Drawing Nanomanufacturing," *Three-Dimensional Nanoarchitectures*, W. Zhou and Z. Wang, eds., Springer, New York, pp. 117–132.

[3] Orf, N. D., Shapira, O., Sorin, F., Danto, S., Baldo, M. A., Joannopoulos, J. D., and Fink, Y., 2011, "Fiber Draw Synthesis," Proc. Natl. Acad. Sci., **108**(12), pp. 4743–4747.

[4] Bayindir, M., Sorin, F., Abouraddy, A. F., Viens, J., Hart, S. D., Joannopoulos, J. D., and Fink, Y., 2004, "Metal-Insulator-Semiconductor Optoelectronic Fibres," Nature, **431**(7010), pp. 826–829.

[5] Bayindir, M., Shapira, O., Saygin-Hinczewski, D., Viens, J., Abouraddy, A. F., Joannopoulos, J. D., and Fink, Y., 2005, "Integrated Fibres for Self-Monitored Optical Transport," Nat. Mater., **4**(11), pp. 820–825.

[6] Bayindir, M., Abouraddy, A. F., Arnold, J., Joannopoulos, J. D., and Fink, Y., 2006, "Thermal-Sensing Fiber Devices by Multimaterial Codrawing," Adv. Mater., **18**(7), pp. 845–849.

[7] Egusa, S., Wang, Z., Chocat, N., Ruff, Z. M., Stolyarov, A. M., Shemuly, D., Sorin, F., Rakich, P. T., Joannopoulos, J. D., and Fink, Y., 2010, "Multimaterial Piezoelectric Fibres," Nat. Mater., **9**(8), pp. 643–648.

[8] Chocat, N., Lestoquoy, G., Wang, Z., Rodgers, D. M., Joannopoulos, J. D., and Fink, Y., 2012, "Piezoelectric Fibers for Conformal Acoustics," Adv. Mater., **24**(39), pp. 5327–5332.

[9] Gumennik, A., Stolyarov, A. M., Schell, B. R., Hou, C., Lestoquoy, G., Sorin, F., McDaniel, W., Rose, A., Joannopoulos, J. D., and Fink, Y., 2012, "All-in-Fiber Chemical Sensing," Adv. Mater., **24**(45), pp. 6005–6009.

[10] Lestoquoy, G., Chocat, N., Wang, Z., Joannopoulos, J. D., and Fink, Y., 2013, "Fabrication and Characterization of Thermally Drawn Fiber Capacitors," Appl. Phys. Lett., **102**(15), p. 152908.

[11] Yaman, M., Khudiyev, T., Ozgur, E., Kanik, M., Aktas, O., Ozgur, E. O., Deniz, H., Korkut, E., and Bayindir, M., 2011, "Arrays of Indefinitely Long Uniform Nanowires and Nanotubes," Nat. Mater., **10**(7), pp. 494–501.

[12] Tuniz, A., Lwin, R., Argyros, A., Fleming, S. C., and Kuhlmey, B. T., 2012, "Fabricating Metamaterials Using the Fiber Drawing Method," J. Visualized Exp., (68), p. e4299.

[13] Alchalaby, A., Lwin, R., Al-Janabi, A. H., Trimby, P. W., Fleming, S. C., Kuhlmey, B. T., and Argyros, A., 2016, "Investigation of Plateau–Rayleigh Instability in Drawn Metal–Polymer Composite Fibers for Metamaterials Fabrication," J. Lightwave Technol., **34**(9), pp. 2198–2205.

[14] Zhao, J., Javadi, A., Lin, T.-C., Hwang, I., Yang, Y., Guan, Z., and Li, X., 2016, "Scalable Manufacturing of Metal Nanoparticles by Thermal Fiber Drawing," ASME J. Micro Nano-Manuf., **4**(4), p. 041002.

[15] Suman, B., and Tandon, P., 2010, "Fluid Flow Stability Analysis of Multilayer Fiber Drawing," Chem. Eng. Sci., **65**(20), pp. 5537–5549.

[16] Jasion, G., Shrimpton, J., Chen, Y., Bradley, T., Richardson, D., and Poletti, F., 2015, "MicroStructure Element Method (MSEM): Viscous Flow Model for the Virtual Draw of Microstructured Optical Fibers," Opt. Express, **23**(1), pp. 312–329.

[17] Pone, E., Dubois, C., Gu, N., Gao, Y., Dupuis, A., Boismenu, F., Lacroix, S., and Skorobogatiy, M., 2006, "Drawing of the Hollow All-Polymer Bragg Fibers," Opt. Express, **14**(13), pp. 5838–5852.

[18] Stokes, Y. M., Buchak, P., Crowdy, D. G., and Ebendorff-Heidepriem, H., 2014, "Drawing of Micro-Structured Fibres: Circular and Non-Circular Tubes," J. Fluid Mech., **755**, pp. 176–203.

[19] Tomotika, S., 1936, "Breaking Up of a Drop of Viscous Liquid Immersed in Another Viscous Fluid Which Is Extending at a Uniform Rate," Proc. R. Soc. London. Ser. A, Math. Phys. Sci., **153**(879), pp. 302–318.

[20] Xue, S., Barton, G. W., Fleming, S., and Argyros, A., 2017, "Analysis of Capillary Instability in Metamaterials Fabrication Using Fibre Drawing Technology," J. Lightwave Technol., **35**(11), pp. 2167–2174.

[21] Xue, S., Barton, G., Fleming, S., and Argyros, A., "Heat Transfer Modelling of the Capillary Fibre Drawing Process," ASME J. Heat Transfer, **139**(7), p. 072001.

[22] Zhang, W. W., 2004, "Viscous Entrainment From a Nozzle: Singular Liquid Spouts," Phys. Rev. Lett., **93**(18), p. 184502.

[23] Ganan-Calvo, A. M., Gonzalez-Prieto, R., Riesco-Chueca, P., Herrada, M. A., and Flores-Mosquera, M., 2007, "Focusing Capillary Jets Close to the Continuum Limit," Nat. Phys., **3**(10), pp. 737–742.

[24] Christopher, G. F., and Anna, S. L., 2007, "Microfluidic Methods for Generating Continuous Droplet Streams," J. Phys. D: Appl. Phys., **40**(19), p. R319.

[25] Yarin, A., Gospodinov, P., Gottlieb, O., and Graham, M., 1999, "Newtonian Glass Fiber Drawing: Chaotic Variation of the Cross-Sectional Radius," Phys. Fluids, **11**(11), pp. 3201–3208.

[26] BASF Corporation, 2017, "Datasheet From Manufacturer (BASF)," BASF Corporation, Wyandotte, MI, accessed Nov. 20, 2017, http://iwww.plasticsportal.com/products/dspdf.php?type=iso&param=Ultrason+E+3010

[27] Wang, L., Wang, Q., Xian, A., and Lu, K., 2003, "Precise Measurement of the Densities of Liquid Bi, Sn, Pb and Sb," J. Phys.: Condens. Matter, **15**(6), p. 777.

[28] Eustathopoulos, N., Nicholas, G., and Drevet, B., 1999, *Wettability at High Temperatures*, Elsevier Science, Oxford , UK.

[29] Gancarz, T., Moser, Z., Gąsior, W., Pstruś, J., and Henein, H., 2011, "A Comparison of Surface Tension, Viscosity, and Density of Sn and Sn–Ag Alloys Using Different Measurement Techniques," Int. J. Thermophys., **32**(6), pp. 1210–1233.

[30] Acrivos, A., and Lo, T., 1978, "Deformation and Breakup of a Single Slender Drop in an Extensional Flow," J. Fluid Mech., **86**(4), pp. 641–672.

[31] Taylor, G., 1934, "The Formation of Emulsions in Definable Fields of Flow," Proc. R. Soc. London. Ser. A, **146**(858), pp. 501–523.
[32] Sherwood, J., 1984, "Tip Streaming From Slender Drops in a Nonlinear Extensional Flow," J. Fluid Mech., **144**, pp. 281–295.
[33] Taroni, M., Breward, C., Cummings, L., and Griffiths, I., 2013, "Asymptotic Solutions of Glass Temperature Profiles During Steady Optical Fibre Drawing," J. Eng. Math., **80**(1), pp. 1–20.
[34] Castro-Hernández, E., Campo-Cortés, F., and Gordillo, J. M., 2012, "Slender-Body Theory for the Generation of Micrometre-Sized Emulsions Through Tip Streaming," J. Fluid Mech., **698**, pp. 423–445.
[35] Gordillo, J. M., Sevilla, A., and Campo-Cortés, F., 2014, "Global Stability of Stretched Jets: Conditions for the Generation of Monodisperse Micro-Emulsions Using Coflows," J. Fluid Mech., **738**, pp. 335–357.
[36] Taylor, G., 1966, "Conical Free Surfaces and Fluid Interfaces," *Applied Mechanics*, Springer, Berlin, pp. 790–796.
[37] Middleman, S., 1977, *Fundamentals of Polymer Processing*, McGraw-Hill, New York.
[38] Birdi, K., Vu, D., and Winter, A., 1988, "Interfacial Tension of Liquids From the Height and Contact Angle of a Single Sessile Drop," Colloid Polym. Sci., **266**(9), pp. 849–854.
[39] Schneider, C. A., Rasband, W. S., and Eliceiri, K. W., 2012, "NIH Image to ImageJ: 25 Years of Image Analysis," Nat. Methods, **9**(7), p. 671.
[40] Stalder, A., Kulik, G., Sage, D., Barbieri, L., and Hoffmann, P., 2006, "A Snake-Based Approach to Accurate Determination of Both Contact Points and Contact Angles," Colloids Surf. A, **286**(1), pp. 92–103.
[41] Reeve, H., and Mescher, A., 2003, "Effect of Unsteady Natural Convection on the Diameter of Drawn Polymer Optical Fiber," Opt. Express, **11**(15), pp. 1770–1779.
[42] Zaporojan, S., Plotnic, C., Calmicov, I., and Larin, V., 2010, *Knowledge-Based Intelligent System Advancements: Systemic and Cybernetic Approaches*, IGI Global, Hershey, PA.